Check for updates

E. coli bacterium tumbling in bulk and close to surfaces: a simulation study†

Pierre Martin, [iD] *[a] Tapan Chandra Adhyapak[b] and Holger Stark [iD] [a]

Motility is fundamental to the survival and proliferation of microorganisms. The *E. coli* bacterium propels itself using a bundle of rotating helical flagella. If one flagellum reverses its rotational direction, it leaves the bundle, performs a polymorphic transformation, and the bacterium tumbles. The *E. coli* bacterium is hydrodynamically attracted to surfaces. This prolongs its residence time, while tumbling facilitates surface detachment. We develop a model of *E. coli* that uses an extended Kirchhoff-rod theory to implement flagellar flexibility as well as different polymorphic conformations and perform hydrodynamic simulations with the method of multi-particle collision dynamics (MPCD). To establish a reference case, we determine the distribution of tumble angles in the bulk fluid. It shows good agreement with experiments, when we always choose the same tumble time. Increasing the hook stiffness, narrows the tumble angle distribution and reduces the flagellar dispersion during tumbling. Close to a bounding surface, the tumble angle distribution is shifted to smaller angles, while flagellar dispersion is reduced. Reorientation within the plane favors the forward direction, which might be an explanation for prolonged run times observed in experiments.

1 Introduction

Bacterial motility is a prerequisite for the survivability and proliferation of bacteria.[1,2] Since the first direct observation of microorganisms,[3] researchers have revealed numerous means of locomotion that bacteria use to swim in a fluid environment at low Reynolds numbers.[4–6] In a real habitat such as the human body but also in a medical catheter or a water pipe, bacteria are not in their planktonic state but they encounter surfaces, where they attach to.[7] This constitutes the onset of the formation of a microcolony, which ultimately develops into complex structures such as a biofilm.[8] The *Escherichia coli* (*E. coli*) bacterium, the most studied microorganism, uses nano-sized rotary motors embedded in its cell wall to propel relatively rigid filaments of helical shape called flagella.[9,10] During a run phase of the bacterium, all flagella rotate in the same direction and form a single tightly packed bundle.[5,11,12] To reorient itself, *E. coli* initiates a tumble event,[13] which serves as the key mechanism for *E. coli* to explore its environment, seek nutrients, or find a surface to attach to and proliferate.[14–16] When approaching a surface, the pusher flow field generated by the bacterium attracts, aligns, and ultimately traps *E. coli* at the surface.[17] A direct consequence is the long residence time of bacteria at surfaces, which facilitates their attachment and the subsequent formation of biofilms.[18,19] As tumbling is also a means for *E. coli* to escape the surface, unraveling how *E. coli* tumbles near surfaces is crucial for understanding bacterial adhesion and could help to develop strategies to mitigate biofilm formation.

A tumble event occurs when one or more flagellar motors reverse their rotation from counterclockwise to clockwise.[11,13] This reversal causes the involved flagella to leave the bundle and undergo a series of polymorphic transitions, starting from the characteristic normal helix shape and transitioning to the final curly-I state.[11,20,21] Once the flagella resume counterclockwise rotation, they transform back to their normal swimming conformation and the bundle reforms. While up to twelve stable polymorphic forms have been predicted,[22] the semi-coiled and curly-I shapes are predominantly observed during tumbling.[11,13] The rotation-induced polymorphic conformations alter key helical properties of the flagella, such as pitch, radius, and handedness.[20,21] These changes modify the steric forces between the flagella as well as the flow fields generated by them, which strongly influences the tumbling process.[21,23,24]

An important part of the bacterial propulsion apparatus is the flagellar hook, a 50–100 nm filament that connects the shaft of the bacterial flagellar motor to the flagellum.[25–27] The hook is a universal joint that efficiently transfers the motor torque to the flagellum regardless of its orientation.[28] The high

[a] *Institute of Physics and Astronomy, Theory Division, Technische Universität Berlin, Hardenbergstrasse 36, 10623 Berlin, Germany.*
  E-mail: p.martin@campus.tu-berlin.de, holger.stark@tu-berlin.de
[b] *Indian Institute of Science Education and Research Tirupati, Yerpedu P.O. PIN 517619, Tirupati, AP, India. E-mail: adhyapak@iisertirupati.ac.in*
† Electronic supplementary information (ESI) available. See DOI: **https://doi.org/10.1039/d5sm00371g**

flexibility of the hook is crucial for the formation of the flagellar bundle[29,30] and its length is tightly regulated by biomolecular mechanisms. Ref. 31 demonstrated that an optimal length is essential for motility. While a shorter hook prevents the formation of the flagellar bundle, a longer hook causes instabilities in the bundle. Although the role of hook flexibility during tumbling is not fully understood, significant variations in its stiffness under rotation have been reported. Ref. 32 finds that the bending stiffness of the hook changes dynamically during rotation, while ref. 33 shows that it increases under clockwise rotation.

A known characteristic of pusher swimmers is their long residence time close to surfaces.[19,34,35] Moreover, chiral microswimmers like *E. coli* perform circular trajectories in the presence of a wall, which limits their exploration capability.[36–38] Tumbling is a key mechanism for the bacterium to escape the surface but also to change swimming direction within the surface. Several experimental studies have investigated the role of tumbling near a flat surface.[39–41] Ref. 39 observed that tumble events mostly reorient bacteria parallel to the wall. In particular, they found that tumbling near a surface causes smaller reorientation angles and occurs at a reduced frequency. So they concluded that tumbling is not very efficient to escape trapping at the surface. In contrast, ref. 41 concluded that tumbling is "a quite efficient means to escape from surfaces" by stressing the large behavioral variability. On the theoretical side, several numerical models have been developed to investigate the swimming *E. coli* close to surfaces.[35,42,43] Furthermore, the few studies that investigated tumbling were all conducted in a bulk fluid.[21,44–46]

To elucidate the specific role of the surface during tumbling, in this article we develop a numerical model of *E. coli* that captures the key features of bacterial motility, including flexible flagella and a full dynamic description of their polymorphism following our earlier work.[20,21] The realistic description of continuous polymorphic transformations during reverse rotation of the flagellum distinguishes us from the work of other groups[44,45] and is more consistent with experimental observations.[13] We use an extended version of the Kirchhoff-rod theory to implement a discrete model for the flexible filament, which has been proven sufficient to capture rotation-induced polymorphic transformations.[20,21,24] The hook is not explicitly modeled, but its universal joint property and high flexibility are preserved. To determine the full hydrodynamic flow field initiated by the moving *E. coli*, we employ the widely used method of multi-particle collision dynamics (MPCD). It has extensively been used over the past two decades and has proven to be successful in resolving the hydrodynamics of microswimmers.[47–51]

In this article, we use the model *E. coli* bacterium to investigate tumbling close to a surface. First, we establish the reference case in the bulk fluid by determining the distribution of tumble angles either for a fixed tumble time or drawn from a Gamma distribution. In particular, for a fixed tumble time good agreement with experiments of Berg and Brown[14] are achieved. Increasing the hook stiffness, narrows the tumble angle distribution and reduces the flagellar dispersion as we

demonstrate by the smallest eigenvalue of the moment of inertia tensor. Close to a bounding surface, we observe that the tumble angle distribution is shifted to smaller angles and reorientation within the plane shows a strong tendency for forward-directed tumbling. Also the flagellar dispersion is reduced.

In Section 2 we introduce the model *E. coli* bacterium and shortly explain the method of multi-particle collision dynamics. In Sections 3 and 4 we present our simulation results of the tumbling *E. coli* first in the bulk fluid and then close to a surface. We also discuss these results and close with conclusions in Section 5.

2 System and simulation method

The *E. coli* bacterium consists of several flagella attached to the cell body. In Section 2.1 we first describe how we model the flagellum using an extended version of the Kirchhoff-rod theory and then in Section 2.2 address the cell body including the motor torque driving a flagellum. The method of multi-particle collision dynamics, which we use to perform the fluid simulations, is introduced in Section 2.3. During the course of explaining our system, we will already mention typical values of our parameters in real units. Then, in Section 2.4 we will formulate them in MPCD units to be used in our simulations.

2.1 Kirchhoff-rod theory to model the flagellum elasticity

The bacterial flagellum is treated as a slender body described by the center-line $\mathbf{r}(s)$ where s is the contour length. We apply the Kirchhoff-rod theory to model its bend and twist elasticity.[52,53] The Frenet–Serret frame $\{\mathbf{e}_1(s),\mathbf{e}_2(s),\mathbf{e}_3(s)\}$, which forms a local orthonormal basis at location s, is used to quantify the deformations of the helix. The vector $\mathbf{e}_3(s)$ represents the local tangent and $\mathbf{e}_1(s)$ and $\mathbf{e}_2(s)$ the cross section of the flagellum. Now, one introduces the rotational strain vector $\boldsymbol{\Omega}$ that transports the material tripod along the centerline,

$$\partial_s \mathbf{e}_\nu = \boldsymbol{\Omega} \times \mathbf{e}_\nu, \quad \nu = 1, 2, 3, \tag{1}$$

where ∂_s means partial derivative with respect to s. The vector $\boldsymbol{\Omega}$ fully characterizes the geometry of the space curve, including the rotation of the cross section about the tangent vector $\mathbf{e}_3(s)$, which represents a twist deformation.[54] In particular, the bacterial flagellum can assume different helical shapes known as polymorphic configurations. They are defined by the ground-state vectors $\boldsymbol{\Omega}^{(n)}$.

A local deformation of the flagellum relative to $\boldsymbol{\Omega}^{(n)}$ is described by $\boldsymbol{\Omega}$. The Kirchhoff free-energy density for the elastic deformation is formulated as a harmonic approximation in $\mathrm{d}\boldsymbol{\Omega} = \boldsymbol{\Omega} - \boldsymbol{\Omega}^{(n)}$,[52]

$$f_K\left(\boldsymbol{\Omega}, \boldsymbol{\Omega}^{(n)}\right) = \frac{A}{2}\left[(\mathrm{d}\Omega_1)^2 + (\mathrm{d}\Omega_2)^2\right] + \frac{C}{2}(\mathrm{d}\Omega_3)^2. \tag{2}$$

Here, A and C are, respectively, the bending and twisting rigidity of the flagellum.

A straightforward generalization of eqn (2) to include the different polymorphic configurations can be achieved by

assigning a ground state energy $\delta^{(n)}$ to each polymorphic form $\mathbf{\Omega}^{(n)}$. Then, the extended version of the Kirchhoff elastic free-energy density is written as[55]

$$f_{EK} = \min_{\forall n}\left[f_K\left(\mathbf{\Omega}, \mathbf{\Omega}^{(n)}\right) + \delta_n\right] + \frac{A}{2}\xi^2(\partial_s\mathbf{\Omega})^2. \quad (3)$$

The first term on the right-hand side of eqn (3) implies that for any rotational strain vector $\mathbf{\Omega}(s)$ at a point s, we choose the ground state vector $\mathbf{\Omega}^{(n)}$ of the lowest energy. As we consider local changes in the elastic energy, the transition between the polymorphic states is smooth and continuous along the flagellum, similarly to what is observed during a tumble event. This is achieved by the last term, which allows a smooth transition between two polymorphic regions of size ξ.[56]

In our model, we allow four polymorphic states involved in a bacterial tumble event, namely normal, coiled, semi-coiled, and curly-I.[11,21,55] The respective ground state vectors $\mathbf{\Omega}^{(n)}$ with components in the local tripod are (in μm^{-1}): {0.00, 1.30, −2.11}, {−0.51, 1.74, −0.56}, {−1.18, 1.84, 0.98}, and {−1.80, 1.56, 2.53}.[55] While E. coli swims in its natural environment, it exhibits the normal configuration. The mechanical and hydrodynamic stresses induced by the reverse rotation of the flagellum cause the polymorphic transitions. Multiple polymorphic states are observed in experiments, where the curly-I helix frequently appears as the final polymorphic shape.[11,13,57] Therefore, we tune the unknown values of the ground state energy $\delta^{(n)}$, which we treat as pure phenomenological parameters, to specifically observe the curly-I state. Studies on how the choice of the ground energies influence the occurrence of different polymorphic shapes were performed in ref. 20 and 21. Since the reversely rotating flagellum leaves the flagellar bundle, the cell body can no longer swim on a straight path. It tumbles and thereby changes its direction. Finally, to maintain a constant length of the filament, a stretching free energy density is added: $f_{st} = K(\partial_s\mathbf{r})^2/2$. Then, the total elastic free energy becomes $\mathscr{F}[\mathbf{r}(s), \Phi(s)] = \int_{C_l}ds(f_{EK} + f_{st})$, where the twist angle $\Phi(s)$ describes a rotation about the local tangent vector $\mathbf{e}_3$.

From this elastic free energy, one can calculate the elastic forces and torques

$$\mathbf{F}_{el} = -\frac{\delta\mathscr{F}}{\delta\mathbf{r}} \text{ and } T_{el} = -\frac{\delta\mathscr{F}}{\delta\Phi} \quad (4)$$

acting locally on the flagellum. A typical length of a flagellum is $C_l = 8 \mu m$. To resolve numerically the flagellar dynamics, the centerline $\mathbf{r}(s)$ is discretized into $N = 80$ beads of mass $M = 10m$ identified by the position $\mathbf{r}_i$, where m is the mass of a single MPCD fluid particle, which we will describe in Section 2.3. $N − 1$ segments connect the beads and carry a Frenet–Serret frame {$\mathbf{e}_1(i), \mathbf{e}_2(i), \mathbf{e}_3(i)$}, the discretized rotational strain vector $\mathbf{\Omega}_i$ describes the rotation of this frame attached to the ith segment. To achieve a suitable hydrodynamic coupling between the flagellum and the fluid, the beads of the flagellum participate in the collision step by exchanging momentum with the solvent, as described in more detail in Section 2.3.

2.2 Physical structure of E. coli

The cell body is constructed using nine overlapping spheres so that they approximately form a spherocylinder. It is treated as a rigid body with a moment of inertia tensor I_{cell} and a density that matches the MPCD fluid, so the cell body is neutrally buoyant. This model has already been demonstrated to be suitable for hydrodynamic studies and is detailed in ref. 50. Standard dimensions for an E. coli cell body are a width of $W = 0.9 \mu m$ and a length of $L = 2.5 \mu m$.[12] The cell body is equipped with an orthonormal basis, {$\mathbf{u}_1, \mathbf{u}_2, \mathbf{u}_3$}, which fully describes its orientation and rotation in space. Four filaments are symmetrically anchored at the rear of the cell body, as illustrated in Fig. 1. This design assumes a fully axisymmetric bacterium. Thereby, the parameter space is considerably reduced. The simplification also allows us to perform systematic studies and to clearly isolate the effect of a surface on the tumbling behavior without the need to randomly choosing the specific position of the reversely rotating flagellum. In a few simulations, we did not see any clear differences in tumbling as long as we placed the flagella at the rear of the cell body. This is an arrangement found in the majority of bacteria as noted in ref. 45. However, when distributing the flagella randomly over the whole cell body, the latter will wobble strongly, which affects swimming and tumbling as reported in ref. 45.

A motor embedded in the cell wall of an E. coli applies a constant torque, which is transmitted through the hook to a flagellum. A motor tripod {$\mathbf{e}_1(0), \mathbf{e}_2(0), \mathbf{e}_3(0)$} with fixed direction of $\mathbf{e}_3(0)$ is placed on the surface of the cell body, so only the rotation around $\mathbf{e}_3(0)$ is allowed. While our simulations cannot numerically resolve the hook, its key physical features are preserved. The motor torque $\mathbf{T}_m$ is constant and applied along the fixed direction $\mathbf{e}_3(0)$ to the flagellum. A counter torque $-\mathbf{T}_m$ is applied to the cell body to satisfy the torque-free condition. The vector $\mathbf{e}_3(0)$ is tilted by an angle $\Theta_m = 55°$ with respect to the bacterium's long axis $\mathbf{u}_3$, as detailed in Fig. 1.[23] This tilt results in a counter-rotation of the cell body at a rate approximately five times slower than that of the bundle, in agreement with experiments.[13] The orthonormal tripod, {$\mathbf{e}_1(0), \mathbf{e}_2(0), \mathbf{e}_3(0)$}, is
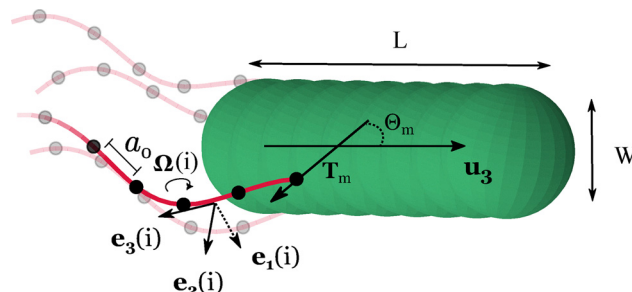

Fig. 1 A schematic of the model bacterium used in our simulations. The cell body has a length L and width W as well as four flagella symmetrically attached at its rear. The motor torque T_m, tilted by an angle Θ_m against the body orientation $\mathbf{u}_3$, drives the motor tripod {$\mathbf{e}_1(0), \mathbf{e}_2(0), \mathbf{e}_3(0)$} (not shown) and thereby it is transmitted to all the tripods {$\mathbf{e}_1(i), \mathbf{e}_2(i), \mathbf{e}_3(i)$} along the flagellum. The rotational strain vector $\mathbf{\Omega}^{(i)}$ transporting tripod i to tripod $i + 1$ is also indicated.

coupled with the rest of the flagellum through the Kirchhoff elastic energy density as described in Section 2.1, but with reduced bending and twisting rigidity.[58] As a result, the motor torque is efficiently transmitted to the flagellum, which can freely bend around the cell body, replicating the physical characteristics of the hook.

To prevent interpenetration between the flagella and the cell body or a bounding surface, steric repulsions are implemented using the WCA potential, an adaptation of the Lennard-Jones potential:

$$U_{\text{WCA}} = \begin{cases} 4\varepsilon\left[\left(\dfrac{\sigma}{r}\right)^{12} - \left(\dfrac{\sigma}{r}\right)^{6}\right] + \varepsilon, & r \leq \sqrt[6]{2}\sigma, \\ 0, & \text{otherwise.} \end{cases} \quad (5)$$

Here, r represents the smallest distance between the flagellum and the nearby surface, while at and beyond the cutoff radius $\sqrt[6]{2}\sigma$ the interaction force is zero. We use U_{WCA} for both flagellum–flagellum and flagellum–cell body interactions, as well as when a bacterium interacts with a wall. For the first case, we have implemented a method so that flagella cannot cross each other as detailed in ref. 23, which also uses U_{WCA}.

2.3 Fluid simulation: multi-particle collision dynamics

The hydrodynamic flow fields initiated by the swimming *E. coli* are determined using the method of multi-particle collision dynamics (MPCD), a coarse-grained particle-based solver of the Navier–Stokes equations.[47,59–61] The MPCD fluid consists of point-like particles with mass m, and their dynamics is resolved through a two-step procedure: the streaming step and the collision step. In the streaming step, each particle performs ballistic motion during time Δt starting from its position $\mathbf{r}_i(t)$ with its velocity $\mathbf{v}_i(t)$:

$$\mathbf{r}_i(t + \Delta t) = \mathbf{r}_i(t) + \mathbf{v}_i(t)\Delta t. \quad (6)$$

In most molecular dynamic simulations, Δt determines the accuracy of the simulation. However, in MPCD Δt is a parameter of the simulation that determines the fluid properties such as the viscosity. In MPCD, particles do not interact directly with each other. Instead, they artificially exchange momentum during the collision step using a collision rule that preserves momentum. In practice, this is realized by sorting particles into unit cells of a cubic lattice with lattice constant a_0. Within a cell ξ, the new velocity $\mathbf{V}_i$ of particle i is calculated according to the special collision rule MPCD AT + a:[62]

$$\mathbf{V}_i = \mathbf{u}_\xi + \mathbf{v}_i^{\text{r}} - \frac{\sum_{j=1}^{N_\xi} m_j \mathbf{v}_j^{\text{r}}}{\sum_{j=1}^{N_\xi} m_j} + \left[\mathbf{I}_\xi^{-1}\sum_{j=1}^{N_\xi} m_j \mathbf{r}_j^{\text{s}} \times \left(\mathbf{v}_j - \mathbf{v}_j^{\text{r}}\right)\right] \times \mathbf{r}_i^{\text{s}}. \quad (7)$$

Here, the velocity $\mathbf{u}_\xi$ represents the mean velocity of fluid particles in cell ξ, and $\mathbf{v}_i^{\text{r}}$ is a random velocity drawn from a Maxwell–Boltzmann distribution at temperature T. The third term is a correction ensuring linear-momentum conservation. The quantity $\mathbf{I}_\xi$ in the last term is the moment of inertia tensor

calculated from the positions of all particles within the cell, and $\mathbf{r}_i^{\text{s}}$ is the relative position of a particle with respect to the cell's center of mass. The last term is needed to ensure angular momentum conservation, which proves to be essential for preserving correct physical behavior.[63] By definition of the collision rule, the temperature remains constant and thermal fluctuations are naturally included. Finally, to ensure Galilean invariance, the grid is randomly shifted at each MPCD step by a vector $\mathbf{s} = \{s_1, s_2, s_3\}$, where the components s_i are drawn from a uniform distribution, $s_i \in \{-a/2, a/2\}$.[64]

When a cubic cell overlaps with the cell body or a wall, virtual particles are introduced within this cubic cell to maintain the average particle density consistent with the surrounding fluid.[61] The virtual particles are important to enhance the accuracy of the hydrodynamic flow field. In particular, they improve the no-slip boundary condition. The mass notation m_j in eqn (7) highlights the distinct mass contributions of the flagellar beads in the collision step.

To couple the bacterium with the solvent, momentum exchange is necessary. Hydrodynamic coupling between the cell body and the fluid is achieved as particles collide with the cell body. They obey the bounce-back rule that reverses the velocities of the colliding particles and thereby enforces the no-slip boundary condition.[47] After the collision, the linear and angular momentum of the cell body are updated by the momenta transferred from the colliding particles to ensure momentum conservation. Similarly, to satisfy the no-slip boundary condition at bounding walls, fluid particles colliding with a wall follow the same bounce-back rule.

2.4 Parameters of the system

All system parameters are expressed in terms of MPCD units, for which we take the lattice constant a_0 as characteristic length, the mass m_0 of the fluid particles, and thermal energy k_BT. Using these parameters, the MPCD time unit is defined as $\tau_0 = a_0\sqrt{m_0/k_BT}$, the viscosity unit as $\eta_0 = \sqrt{m_0 k_BT}/a_0^2$, and the resulting velocity unit becomes $v_0 = \sqrt{k_BT/m_0}$. In our simulations, the density of MPCD particles is set to $\rho = 10/a_0^3$ and the MPCD time step is $\Delta t = 0.05\tau_0$. These quantities together with the specific collision rule determine the viscosity, which becomes $\eta = 7.5\eta_0$.[65] The thermal energy is $k_BT = 4.13$ pN nm at room temperature $T = 300$ K.

To have a good balance between computational efficiency and good resolution of our model bacterium, we match its dimension with *E. coli* and set the lattice constant to $a_0 = 0.1$ μm. By comparing with the real values mentioned in the previous sections, we can then fix all lengths in units of a_0. During a typical simulation of a tumble event, the bacterium is immersed in a cubic box with periodic boundaries of size $L_b = 150a_0$, approximately twice the size of the modeled bacterium and sufficiently large to mitigate reflections of the flow field at the boundaries. The cell body has a width and length given by $W = 9a_0$ and $L = 25a_0$, respectively. The length of a flagellum is set to $80a_0$ and the number of 80 beads are chosen such that in each cell one has a bead with mass $M = 10m_0$, which ensures

matching density with the solvent.[61,66] Therefore, in the simulations the segments connecting the beads have a length of a_0. For the width of the flagellum, which appears as σ in the WCA potential of eqn (5) for flagellum–flagellum and flagellum–cell body interactions, we choose $\sigma = 0.4a_0$, roughly twice the real width. When the bacterium interacts with a wall, we use $\sigma = a_0$. Finally, the energy unit in the WCA potential is set to $\varepsilon = k_B T$.

The other physical parameters of the flagellum are also chosen to be consistent with experimental observations. The magnitude of the motor torque applied to the flagellum is constant and set to $|\mathbf{T}_m| = 820k_B T$, which leads to an average velocity $v \approx 0.03v_0$.[13,20,23]

The bending and twisting rigidities of the flagellum are, respectively, $A = 13\,310k_B Ta_0$ and $C = 8450k_B Ta_0$.[13,67] To prevent elongation of the flagellum, a high stretching rigidity, $K = 10^5 k_B T/a_0$ is applied. As discussed in Section 2.2, the values of the ground state energies are fixed and set to $\delta^{(n)} = \{0.0, 25, 10, 0.0\}$ in units of $k_B T$. The values are chosen such that during reverse rotation the flagellum reaches the fourth, the curly-I state. Although the bending rigidity of the hook varies dynamically,[32,33] we simplify the model by assuming it remains constant at $A_h = 2.5k_B Ta_0$ with the twisting rigidity set to $C_h = 4840k_B Ta_0$.[21,68]

With the chosen parameters, the time scale for vorticity diffusion is $\tau_d = \rho W^2/\eta \approx 100\tau_0$,[69] and the Reynolds number becomes $\mathrm{Re} = \rho W v/\eta \approx 0.4$, where v is the swimming velocity.‡ For each simulation of a tumble event the bacterium is first left to swim for a random number of MPCD steps such that the time is larger than τ_d. This ensures that the flow field has been fully established and also reduces correlations between successive simulations, when determining the distributions of tumble angles.

Finally, mapping the viscosity η in the MPCD simulations to that of water, results in a bundle rotation frequency $2\pi\omega \approx 600$ Hz and a swimming velocity $v \approx 100$ μm s^{-1}. Although these values are higher than those observed in experiments, the ratio $v/\omega r \approx 0.1$, where $r = 0.2$ μm refers to the helical radius of the normal flagellar configuration, is consistent with experimental findings.[13]

3 Tumbling *E. coli* in a bulk fluid

We start with describing a tumbling *E. coli* in a bulk fluid to have a reference case for the investigations in Section 4, where we consider tumbling close to a surface. In Section 3.1 we introduce a single tumble event, either with fixed tumble time or drawn from a Gamma distribution, and then describe a typical event in detail. Then, in Section 3.2 we show a long trajectory of a running and tumbling bacterium with run and tumble times drawn from respective Gamma distributions.

‡ Such values of the Reynolds number are typical for MPCD simulations of low-Reynolds-number hydrodynamics.[35,48,51] This is due to the viscosity of the MPCD fluid, which is much smaller than that of water. The viscosity is regulated by the time step Δt, which would need to be 60 times smaller than in our simulations, making them prohibitively long.

Finally, in Section 3.3 we characterize the tumble events by discussing tumble angle distributions, the influence of hook bending rigidity, and the flagellar dispersion during tumbling.

3.1 Description of a tumble event

The duration of a tumble event of *E. coli* typically ranges between 0.1 and 0.3 s.[14,70,71] In our model, a tumble event is triggered by reversing the direction of the motor torque. In the following, we take the tumble duration τ_t as the time during which the reverse torque is applied. We express this duration in terms of the period of the bundle rotation, τ_b. The flagellar bundle of an *E. coli* typically rotates at a frequency of 100 Hz.[13] Thus the tumble duration of 0.3 s, corresponds to $30\tau_b$. We investigate two cases. In the first scenario, the tumble time assumes the fixed value $\tau_t = 30\tau_b$. In the second scenario, we allow the tumble time to vary, as observed in experiments. We assume that it follows a Gamma distribution

$$P(\tau_t; k, \theta) = \frac{1}{\Gamma(k)\theta^k}\tau_t^{k-1}e^{-\tau_t/\theta} \text{ with } \Gamma(k) = (k-1)! \qquad (8)$$

where k and θ are the shape and scale parameters, respectively. We chose $k = 2$ and the $\theta = 15\tau_b$, which gives a mean tumble time of $\langle \tau_t \rangle = 30\tau_b$. In particular, the distribution grows linearly at small τ_t. The use of the Gamma distribution is motivated by experimental observations in ref. 41.

A tumble is initiated by reversing the rotational direction of one flagellum. For this, the torque is linearly switched in time from $-T_m$ to T_m over a short period of $3.5\tau_b$. The finite-time transition is motivated both by a realistic representation of the bacterial flagellar motor and by numerical stability. Considering a tumble time of 0.3 s, the switching time is 35 ms, which is in the range of values found in ref. 72 and which also ensures numerical stability of the transition. Once the tumbling time has elapsed, the torque is smoothly reversed back to $-T_m$ during time $3.5\tau_b$.

A typical tumble event with a tumble duration of $30\tau_b$ is illustrated by snapshots from our simulations in Fig. 2 and Video A1 (ESI†). Different phases can be distinguished. The first phase lasts until $t = 15\tau_b$. It starts with initiating the reverse rotation so that the flagellum switches from the normal (red) to
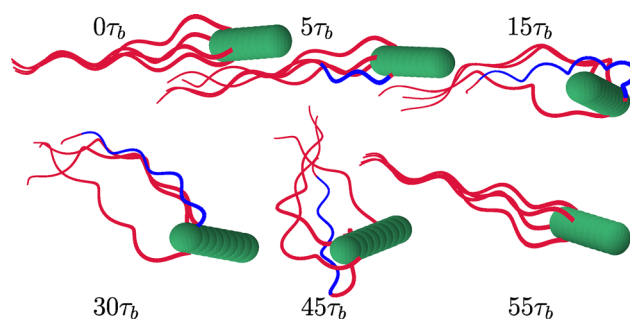

Fig. 2 Simulation snapshots of a tumble event at different time points. The flagellum shown in red represents the normal helical configuration, while in the reversely rotating flagellum blue indicates the transition to the curly-I state propagating along the flagellum. The reverse rotation starts at $0\tau_b$ and ends at $30\tau_b$, as detailed in the main text.

the curly-I (blue) configuration. The viscous drag on the reversely rotating flagellum initiates a reversal of the local helical torsion so that the transition to the curly-I state rapidly propagates from the cell body to the tip of the flagellum covering 95% of its full length. The speed and extent of this transition strongly depends on the ground state energies $\delta^{(n)}$ and the motor torque.[20,21] Interestingly, when initiating the transition to the curly-I state, the flagellum hardly rotates while the other flagella push the cell body forward so that it always tilts towards the transforming flagellum (see Fig. 2, snapshot at $t = 5\tau_b$). In the second phase, $15\tau_b < t < 30\tau_b$, we observe that in most cases the flagellar bundle disintegrates and the single filaments buckle. The reversely rotating flagellum either leaves the remaining part of the bundle or stays entangled. In both case, the propelling structure is largely dispersed as shown in Fig. 2. Note that our simulations deviate here from the typical representation of a tumble event that shows the reversely rotating flagellum outside an intact bundle.[13] However, experimental observations also reveal a diverse behavior of the bundle during tumbling reminiscent of our simulations.[11,41,73] Finally, once the motor torque has reversed back, in the time period $30\tau_b < t < 55\tau_b$ the flagellum transitions from the curly-I configuration to the normal state and the bundle forms again. Note that our formal definition of the tumble duration as the time between two reversals of the motor torque does not fully reflect the duration of a tumble event, since the reformation of the bundle also takes time.
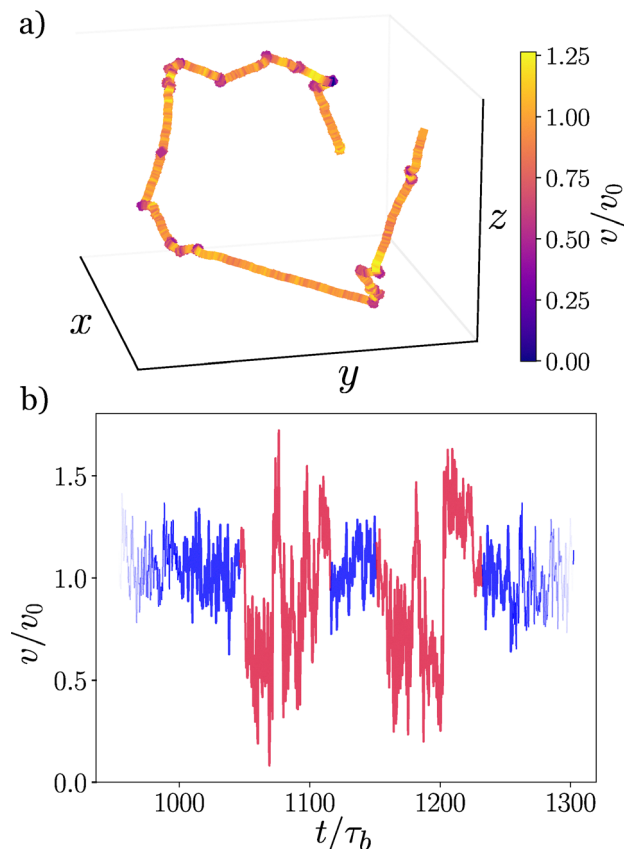
We simulated a large number of single tumble events. To quantify the reorientation of the swimming *E. coli* bacterium, we defined the tumble angle γ as

$$\gamma = \arccos(\hat{\mathbf{u}}_i \cdot \hat{\mathbf{u}}_f). \qquad (9)$$

Here, the unit vector $\hat{\mathbf{u}}_i$ describes the swimming direction or orientation of the bacterium before reversing the rotation of a motor torque, while $\hat{\mathbf{u}}_f$ refers to the orientation once the flagella are fully rebundled. To avoid strong influences from the wobbling cell body on the tumble angle, we adopted a more robust definition of orientation by taking the orientation vector from the center of mass of the bundle to that of the cell body, which we average over several snapshots taken from the simulations.

3.2 Long trajectory: an *E. coli* runs and tumbles

We also simulated long trajectories of the tumbling *E. coli* with a total duration of $1455\tau_b$. The bacterium is immersed into an unbounded MPCD fluid with periodic boundary conditions and moves through alternating run and tumble phases. The durations of both phases follow here the Gamma distribution of eqn (8) with respective mean run and tumble times of $90\tau_b$ and $30\tau_b$. Fig. 3(a) illustrates the trajectory of the simulated *E. coli* bacterium. During the run phase, all the flagellar motors rotate in the same direction. Hydrodynamic and steric interactions synchronize the rotation of the flagella so that they form a bundle. Its helical structure drives the cell body in a nearly

Fig. 3 (a) Long simulated trajectory of the *E. coli* bacterium. Both, the run and the tumble durations are taken from Gamma distributions, with respective mean run and tumble times of $90\tau_b$ and $30\tau_b$. The color map quantifies the velocity of the bacterium normalized by the swimming velocity v_0. Dark blue indicates a drop of velocity corresponding to a tumble event. (b) Swimming velocity of the bacterium plotted *versus* time taken from the trajectory in (a) for two tumble events. The blue and red color represent the velocities during running and tumbling phase, respectively.

straight trajectory with a constant swimming velocity v_0. Small changes in the direction are due to rotational diffusion.[12]

The color map in Fig. 3(a) represents the swimming velocity of the bacterium along the trajectory. We define it as

$$v = \mathbf{v}_G \cdot \hat{\mathbf{u}} \qquad (10)$$

where $\mathbf{v}_G$ is the velocity of the midpoint between the centers of mass of the bundle and the cell body, and $\hat{\mathbf{u}}$ is the orientation vector connecting both centers of mass. Before each change in direction, the color code indicates a decrease in velocity. Note that towards the end of the trajectory a tumble event occurs with nearly no change in the swimming direction.
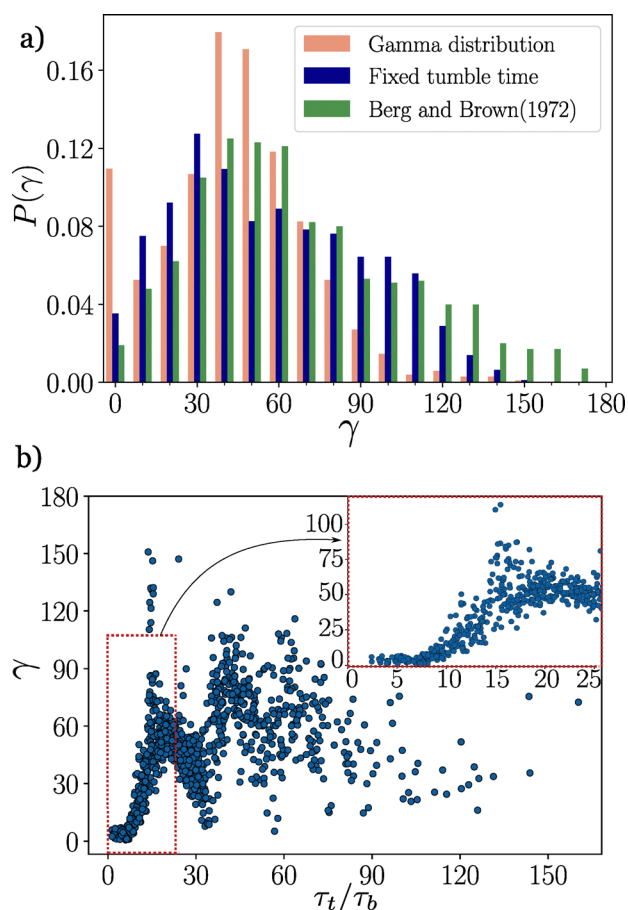
Fig. 3(b) provides a detailed account of the instantaneous velocity. During the tumbling phase (indicated in red), the velocity decreases, but it also strongly fluctuates. The mean velocity during tumbling is $\langle v_t \rangle = 0.8v_0$, where $v_0 = \langle v_r \rangle$ is the mean velocity during the run phase. The standard deviation of the fluctuations amounts to $\Delta v_t = 0.3v_0$, considerably larger than the standard deviation in the run phase, $\Delta v_r = 0.1v_0$. These large fluctuations

are the cause that $\langle v_t \rangle$ is not smaller. We comment on them further. As described in the previous subsection, the flagella are misaligned with the cell body and exhibit strong buckling. This deformation of the helical structure results in irregular propulsive forces acting from the rotating flagella onto the cell body, which thereby performs erratic changes in its orientation as illustrated in Fig. 2. This can also give rise to a sudden increase of velocity beyond v_0, which is visible in Fig. 3(b). Finally, once the flagellum reverts back and the bundle reforms, the cell body resumes swimming at a constant velocity v_0.

3.3 Analysis of the tumble event

How much the bacterium reorients during a tumble event varies significantly both in experiments and our simulations. To quantify this, we present in Fig. 4(a) the distribution $P(\gamma)$ of the tumble angle for simulations where the tumble time τ_t was either fixed (blue) or chosen from the Gamma distribution $P(\tau_t;2,15\tau_b)$ of eqn (8) (salmon). The distributions were obtained from 932 or 1032 independent simulations,

Fig. 4 (a) Bar plot of the probability distribution $P(\gamma)$ of the tumble angle γ. The green data points are reproduced from ref. 14. The blue and salmon data points belong to simulations, where the tumble time τ_t was either fixed or chosen from the Gamma distribution $P(\tau_t;2,15\tau_b)$ of eqn (8), respectively. (b) Tumble angle γ plotted *versus* tumble time τ_t chosen from $P(\tau_t;2,15\tau_b)$. The red frame highlights the region for small τ_t shown in the inset.

respectively. For a fixed tumble time, $P(\gamma)$ with mean tumble angle $\langle \gamma \rangle = 61°$ and a standard deviation of $\Delta\gamma = 34°$ is in good agreement with the measurements of Berg and Brown in ref. 14, where they obtained $\langle \gamma \rangle = 62°$ and $\Delta\gamma = 26°$.

The tumble angle distribution for tumble times chosen from a Gamma distribution roughly reproduces the most probable tumble angle in the experiments but does not reach to large tumble angles. As a result the mean tumble angle of 49° is smaller while $\Delta\gamma = 27°$ is comparable to the previous values. Most prominently, a peak appears for angles between 0° and 10°, which results from short tumble events. This is illustrated in Fig. 4(b), where we correlate tumble angle with tumble time. The inset shows that a noticeable reorientation of *E. coli* only occurs at times larger than $10\tau_b$. Prior to this time, the reversely rotated flagellum is not fully transformed into the curly-I state and the bundle is still intact (see Fig. 2). Therefore, such tumble events, for which we show an example in Video A2 (ESI†), might have been overlooked in experiments and their small tumble angles not recorded.

For tumble times $10\tau_b < \tau_t < 15\tau_b$, there is a nearly one-to-one relation between tumble angle and tumble time meaning the bacterium moves deterministically. Then, around $\tau_t \sim 15\tau_b$ the tumble angle spreads widely and even reaches very large values at $\tau_t \approx 15\tau_b$. This behavior is due to the hook's high flexibility, which enables the cell body to rotate freely so that it no longer moves deterministically. In particular, at $\tau_t \approx 15\tau_b$ cell body and flagella point in opposite directions. Finally, as the tumble time extends beyond $\tau_t \sim 30\tau_b$, the tumble angle becomes increasingly scattered, although we always use the same attachment points for all four flagella. This shows the complex interplay of hydrodynamic forces, flagellar elasticity, and cell body dynamics. Together, these factors give rise to a highly dynamic and intricate reorientation process.

Recent studies have shown that the stiffness of the hook strongly increases with angular velocity of the motor.[32,33] To capture the role of hook flexibility during a tumble event, we increase its bending rigidity A_h by a factor of 10, 100, and 400, respectively, such that it is still at least one order of magnitude smaller than the flagellar bending rigidity. Furthermore, we choose a fixed tumble time in the simulations. As shown in ref. 29 and 31, hook stiffness plays a crucial role in the motility of *E. coli* since an increased stiffness prevented the formation of the bundle. In our simulations we made sure that the flagella still formed a bundle prior to a tumble event, for all the chosen rigidities.

Fig. 5 shows the tumble angle distribution $P(\gamma)$ for the three hook bending rigidities, mentioned above. The distributions are constructed from independent simulations, with a total of 570, 346, and 624 simulations for the respective rigidities $10A_h$, $100A_h$, and $400A_h$. For a hook bending rigidity of $10A_h$ only small changes occur relative to the reference case A_h. Therefore, we do not show the latter in Fig. 5. However, for rigidities of $100A_h$ and $400A_h$, the distributions become more narrow and only tumble angles between 20° and 120° do mainly occur. The respective mean tumble angles of 87° and 69° are above the value of 61° for the reference case, while the respective standard
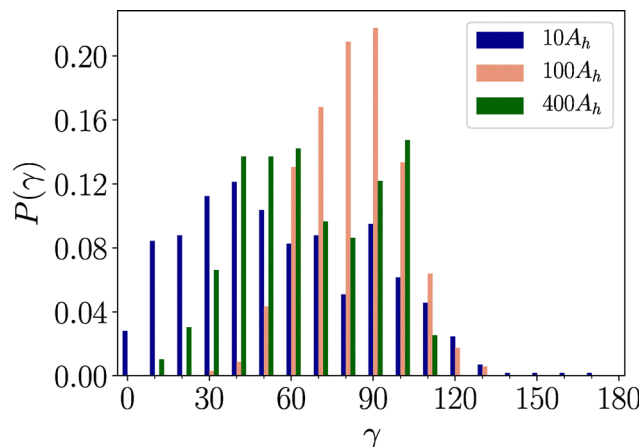
Fig. 5 Bar plot of the probability distribution $P(\gamma)$ for three different values of the hook bending rigidity. The fixed tumble time $\tau_t = 30\tau_b$ is used in the simulations.

Fig. 6 Scatter plots of the tumble angle γ *versus* time-averaged moment of inertia I_1/I_1^{bundle} for different values of hook bending rigidity. The red dashed lines highlight the mean value $\langle I_1 \rangle/I_1^{\text{bundle}}$. Cases shown in Videos A1 and A5 (ESI†) are indicated by red circles.

deviations of 17.4° and 24.7° are below 34° measured for the reference case. The significant changes observed in the tumble angle distribution can be attributed to the mechanical constraints imposed on the cell body by a rigid hook. In the case of a flexible hook, the cell body is free to rotate around the flagellum during a tumble event, as previously discussed together with Fig. 2. The bending forces between the hook and the cell body are too weak to restrict this motion. However, when the hook becomes sufficiently rigid, these bending forces become strong enough to mechanically constrain the rotation of the cell body, which might be the reason for the more narrow distributions. Although the rotational restriction is observed for both $100A_h$ and $400A_h$, their tumble angle distributions differ significantly. We argue below that these variations can be explained by differences in flagellar dispersion. Moreover, the Videos A3 and A4 (ESI†) show that the increased hook bending rigidity more and more impairs the rotation of the reversely rotating flagellum. Therefore, the friction forces are significantly reduced and the polymorphic transformation to the curly-I state is delayed. For a hook rigidity of $1000A_h$ the motor stalls completely and the polymorphic transition no longer occurs. These observations emphasize the key role of the hook bending rigidity in the bacterial motility, affecting directly the tumble angle distribution. Our simulations also reveal that the increased hook bending rigidity significantly reduces the dispersion of the flagellar bundle during tumbling.

To quantify the flagellar dispersion, we calculate the moment of inertia tensor **I** of the bundle,

$$I_{ij} = m \sum_{k=1}^{N} \left(\left| \mathbf{r}^{(k)} \right|^2 \delta_{ij} - x_i^{(k)} x_j^{(k)} \right), \qquad (11)$$

where N is the number of beads with mass m forming the four flagella, $\mathbf{r}^{(k)} = (x_1^{(k)}, x_2^{(k)}, x_3^{(k)})$ the position vector of bead k taken relative to the center of mass of the bundle, and δ_{ij} the Kronecker delta. We calculate the eigenvectors and eigenvalues of **I** that provide the main rotational axes and moments of inertia of the flagellar bundle. For an intact bundle, the smallest eigenvalue I_1^{bundle} refers to rotations about the bundle axis. To
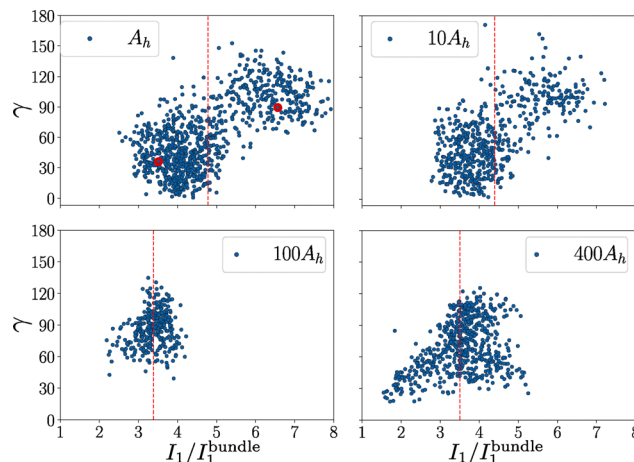
quantify the dispersion of the bundle during a tumble event, we use the time average of the smallest eigenvalue over a complete tumble event and denote it with I_1. The tumble event begins at the reverse rotation of the motor and ends once the flagella have fully rebundled. Thus, a value of I_1 larger than I_1^{bundle} measures the flagellar dispersion.

In Fig. 6 we show scatter plots for all the tumble events that were used in Fig. 4(a) and 5 for different hook bending rigidities. They reveal correlations of I_1/I_1^{bundle} with the tumble angle γ. The dashed lines show the mean values of I_1/I_1^{bundle} averaged over all tumble events. One immediately recognizes that increasing the hook bending rigidity significantly reduces the flagellar dispersion, meaning $\langle I_1 \rangle/I_1^{\text{bundle}}$ decreases.

For hook bending rigidities A_h and $10A_h$ we discern two distinct regions. Tumble angles between 0° and 90° belong to smaller I_1, while tumble angles above 90° clearly correlate with large I_1. We illustrate the two cases with videos for rigidity A_h. Video A1 (ESI†), which corresponds to the tumble event illustrated in Fig. 2, shows a small flagellar dispersion $I_1/I_1^{\text{bundle}} = 3.5$ and a tumble angle $\gamma = 32°$. The flagellar bundle spreads and separates into two distinct parts, with one flagellum (not necessarily reversely rotating) separated from the others. In contrast, Video A5 (ESI†) illustrates the large dispersion case with $I_1/I_1^{\text{bundle}} = 6.6$ and $\gamma = 92.8°$. Interestingly, the bundle remains tightly packed throughout the entire tumble phase but then fully unbundles once the motor of the fourth flagellum reverses back. At this moment, the cell body is roughly anti-parallel to all the flagella and to unit all of them in a single bundle behind the cell body, they first have to fully unbundle.

At hook bending rigidities of $100A_h$ and $400A_h$, the mean value $\langle I_1 \rangle/I_1^{\text{bundle}}$ is significantly reduced and tumble angles above 120° hardly occur. The reason is that the bundle formed by the three flagella remains nearly intact during tumbling as the Videos A3 and A4 (ESI†) show.

Nevertheless, the case of $400A_h$ exhibits more variability in I_1 compared to $100A_h$. One possible explanation is that the

reversely rotating flagellum can protrude further from the cell body. We suggest that this difference in flagellar dispersion explains the different tumble angle distributions in Fig. 5: more peaked for the case of $100A_h$ and more scattered for $400A_h$. Furthermore, as we already noted, the reversely rotating flagellum is strongly impaired by the increased bending rigidity of the hook, which delays the polymorphic transition to the curly-I state. In contrast to the previous case, the larger hook rigidity also impairs the free rotation of the cell body relative to all the flagella, since the stiffer hook acts with a torque on the cell body. It therefore reorients less and large tumble angles do not occur. Note, for the rigidity of $400A_h$ the bundle stays even more compact compared to the rigidity of $100A_h$ and the reversely rotating flagella protrudes more strongly from the cell body (see Videos A3 and A4, ESI†). This is very reminiscent of the typical description of a tumble event in experiments.[13]

4 Tumbling *E. coli* close to a flat surface

This section performs the same type of analysis as described in Section 3 but now with the *E. coli* moving in the proximity of a flat surface. Section 4.1 presents the simulation of an extended trajectory of the *E. coli* using the same run and tumble characteristics as in Section 3.2. Then, Section 4.2 analyzes tumble events near the surface and compares the tumble angle probability distribution $P(\gamma)$ to the bulk case. It also introduces the in-plane angle ϕ and the polar angle θ as well as their distributions to characterize the reorientation of the *E. coli* close to the surface. Finally, we relate these angles also to the dispersion of the flagellar bundle during tumbling.

4.1 Long trajectory: an *E. coli* close to a flat surface

As a bacterium leaves the bulk fluid, it swims towards and hits a bounding surface,[34] where steric as well as hydrodynamic interactions with the surface reorient the bacterium.[17,34] Ultimately, the bacterium becomes trapped by hydrodynamic interactions[17] and follows a circular trajectory that significantly reduces its exploration capability.[36,42] In Appendix A we show that a non-tumbling bacterium performs a circular trajectory as observed in experiments.[36–38] In contrast, tumbling serves as a key mechanism for bacteria to escape from the surface. Similar to Section 3.2, we simulated a long trajectory over a duration of $1400\tau_b$, where run and tumble times were drawn from the same Gamma distributions as in the bulk fluid. Two parallel no-slip walls, with distance $150a_0$ and the normal pointing along the z direction, bound the fluid, while periodic boundary conditions are applied in the x and y directions, respectively.

When we simulate a long trajectory of the bacterium, eventually, it orients towards and reaches one surface. This is illustrated from different perspectives in Fig. 7, where we show a segment of the long trajectory. Along the bacterial path we record nine tumble events, each marked by a drop in swimming velocity as in the bulk fluid and in agreement with experimental observations.[40] Initially, the bacterium swims towards the
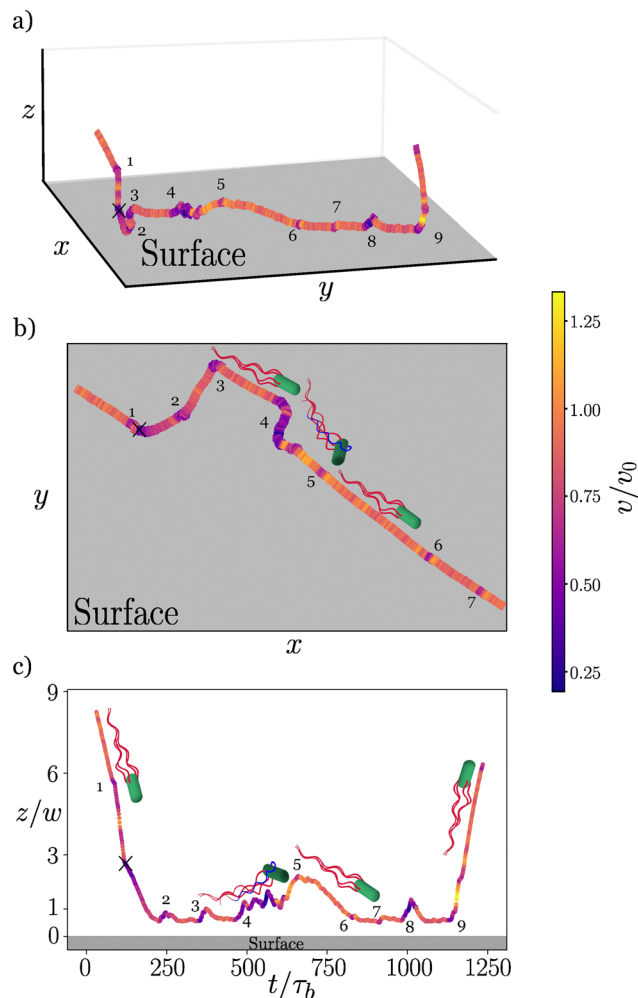

Fig. 7 Run and tumble trajectory of the center of mass of an *E. coli* close to a surface shown from different perspectives. The numbers enumerate and locate the successive tumble events. The black cross between 1 and 2 indicates where the bacterium collides with the surface. The color map records the change in the swimming velocity. (a) Three-dimensional representation of the trajectory starting on the left. The bottom surface is colored in grey to emphasize the bacterium's proximity to it. (b) Top view and (c) side view. The distance z to the surface as a function of time is rescaled with the width w of the cell body to highlight its proximity to the wall.

surface and undergoes one tumble event in the bulk fluid [event 1 in Fig. 7(c)]. Then, it collides with the wall, which we mark by a cross on the trajectory. This shows that hydrodynamic reorientation due to the presence of a wall is not sufficient to prevent the collision,[17,34] which is consistent with simulations in ref. 35. Once near the surface, the bacterium swims parallel to it and goes through several tumble events (2 to 9 in Fig. 7). Thus, a total of eight tumbles are necessary to successfully reorient away from the wall and leave the surface. This highlights that the *E. coli* bacterium preferentially reorients parallel to a bounding surface during tumbling. In addition, the top-down view of Fig. 7(b) shows that the in-plane reorientation can also be relatively small. Of course, as illustrated in Fig. 4 a small reorientation is also caused by the short

duration of the reversely rotating flagellum. However, as we show in the following, it is a specific feature of tumbling close to a surface.

4.2 Analysis of the tumble event

To further investigate tumbling close to a surface as apparent in Fig. 7, we perform independent simulations of single tumble events, where we fix the reverse rotation of one flagellum to the constant time $\tau_t = 30\tau_b$, as before in the bulk fluid. For each simulation, the bacterium is placed close to and parallel to the surface so that it swims at a steady height.[35,42] Then, tumbling is initiated by reversing the rotation of one flagellum, as described in Section 2.4. Videos A6 (side view) and A7 (ESI†) (top view) show a typical tumble event close to a surface. Fig. 8(a) compares the tumble angle distributions $P(\gamma)$ in the bulk fluid and close to the surface. There, the distribution is clearly strongly shifted towards smaller tumble angles with a mean value $\langle\gamma\rangle = 41°$ and a standard deviation $\Delta\gamma = 32°$. In the bulk fluid the respective values were $\langle\gamma\rangle = 61°$ and $\Delta\gamma = 34°$.

To better characterize the orientation of the bacterium after tumbling, we calculate the polar (θ) and in-plane (ϕ) reorientation angles as illustrated in the inset of Fig. 8(b),

$$\theta = \arccos(\hat{\mathbf{z}} \cdot \hat{\mathbf{u}}_f), \quad \phi = \arccos\left(\frac{\hat{\mathbf{u}}_i^{\perp} \cdot \hat{\mathbf{u}}_f^{\perp}}{|\hat{\mathbf{u}}_i^{\perp}||\hat{\mathbf{u}}_f^{\perp}|}\right). \quad (12)$$
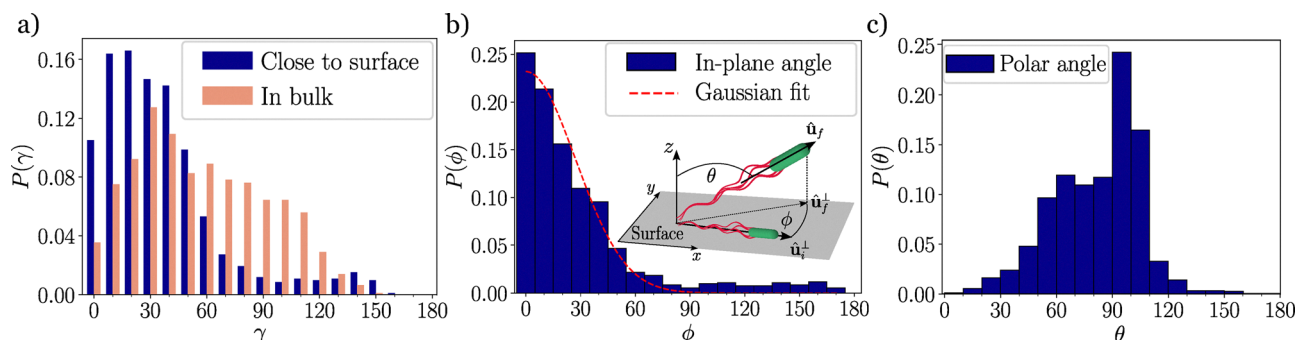
Here, $\hat{\mathbf{z}}$ is the unit vector normal to the surface and $\mathbf{u}_i^{\perp}$, $\mathbf{u}_f^{\perp}$ are the respective projections of the initial ($\mathbf{u}_i$) and final ($\mathbf{u}_f$) orientation vectors on the surface.

The in-plane tumble angle distribution $P(\phi)$ plotted in Fig. 8(b) shows a strong tendency for forward-directed tumbling with small in-plane reorientation. In fact, 25% of the recorded tumble events show an in-plane angle smaller than 10°. This observation aligns with the simulated long trajectory in Fig. 7(b), which demonstrates that tumble events often result in small in-plane reorientations as illustrated by Video A7 (ESI†). Interestingly, $P(\phi)$ can be modeled by enhanced orientational diffusion in two dimensions as the fit with the normal distribution $\mathcal{N}(0, \sqrt{2D_T\tau_t})$ in Fig. 8(b) shows.[71,74] The fitted

rotational diffusion constant $D_T \approx 3$ s^{-1} for the duration $\tau_t = 30\tau_b$ of a tumble event is in good agreement with our previous results.[71] The experimental study of ref. 39 reports a reduced frequency of tumble events near a surface and concludes that a surface suppresses tumbling. In contrast, our simulations indicate that in-plane reorientation is small [Fig. 8(b)] and, therefore, such events might have been overlooked in the experiments. In fact, the trajectory in ref. 39 shows events with a strong decrease in velocity, which are not documented as tumbling.
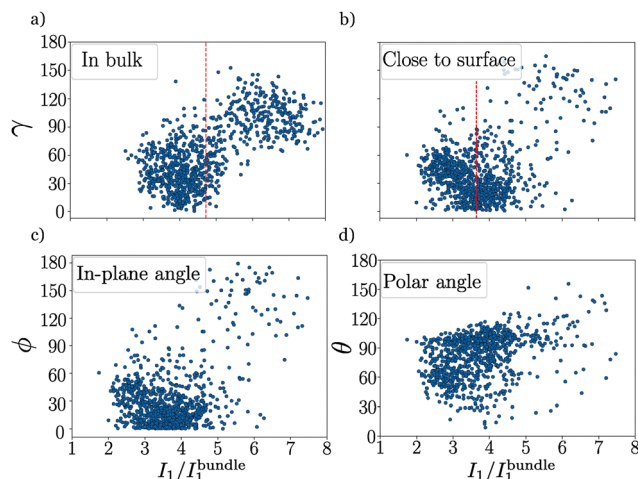
The distribution of the polar reorientation angle is shown in Fig. 8(c). It peaks around $\theta = 90°$, which is consistent with our observations of long trajectories at the surface (Fig. 7) and with experimental findings.[39,41] The experiments show that after tumbling near a surface, bacteria tend to reorient parallel to it. We can also deduce the escape rate from $P(\theta)$, as a polar angle θ smaller than 90° means that the bacterium is oriented away from the surface. Our analysis reveals that 53% of tumble events result in the bacterium swimming away from the surface. But it does not necessarily fully escape as the side view of the trajectory in Fig. 7(c) illustrates. An example of an escaping bacterium is shown in Video A8 (ESI†).

As in Section 3.3, we determine the smallest eigenvalue I_1 of the moment of inertia tensor of the four flagella and use it as a measure for the dispersion of the flagellar bundle during tumbling. We correlate it with the tumble angle γ in Fig. 9(a) and (b) that contain the scatter plots for the bulk fluid and close to a flat surface, respectively. Video A8 (ESI†) shows a tumble event with small dispersion $I_1/I_1^{\text{bundle}} = 2.5$ and a tumble angle $\gamma = 35°$, while Video A9 (ESI†) illustrates the case of large dispersion with $I_1/I_1^{\text{bundle}} = 5.7$ and $\gamma = 140°$. Close to a surface, one still recognizes two regions in the scatter plot, but the tumble events with large dispersions and large tumble angles are less frequent. As a result, the mean dispersion quantified by the mean value $\langle I_1\rangle/I_1^{\text{bundle}}$ is significantly smaller near the surface. In the bulk fluid, large bundle dispersion predominantly is correlated with strong reorientation. This is still true near a surface, but small tumble angles can also arise. In total, reorientations with smaller tumble angles dominate and are

Fig. 8 Bar plots of the probability distributions of different reorientation angles during tumble events: (a) comparison between tumble angle distributions $P(\gamma)$ in bulk and close to a surface, drawn in salmon and blue color, respectively. (b) Distribution $P(\phi)$ of the in-plane reorientation angle ϕ and a fit by the normal distribution $\mathcal{N}(0, \sqrt{2D_T\tau_t})$ with tumble time $\tau_t = 30\tau_b$ and fitted rotational diffusion constant $D_T \approx 3$ s^{-1}. Inset: Definition of the reorientation angles ϕ, θ. $\hat{u}_i^{\perp}$ and $\hat{u}_f^{\perp}$ are the respective projections of the initial ($\hat{u}_i$) and final ($\hat{u}_f$) orientation vectors on the surface. (c) Distribution $P(\theta)$ of the polar reorientation angle θ measured relative to the surface normal, see inset of (b).

Fig. 9 Several scatter plots correlating the reorientation of the bacterium due to tumbling with the time-averaged moment of inertia I_1/I_1^{bundle}: tumble angle (a) in bulk and (b) near a surface, where the red dashed lines highlight the mean value of I_1/I_1^{bundle}. (c) In-plane angle and (d) polar angle.

coupled to tighter bundles with lower dispersion. In Appendix B we show that during a tumble event the flagella frequently collide or directly interact with the surface. We identify this as the main cause for the reduced bundle dispersion. The enhanced flagellar drag due to the presence of a wall should have a minor effect.

Fig. 9(c) shows the scatter plot relating in-plane reorientation angle and flagellar dispersion. It is comparable to the scatter plot of the tumble angle γ in (b), where small reorientation mainly correlates with small dispersion. In contrast, although less frequent at the surface, the large in-plane reorientation events are mainly due to increased flagellar dispersion. Nevertheless, they may help to explore the surface, which otherwise is limited due to circular swimming.[36,37]

Finally, Fig. 9(d) presents the scatter plot for the polar angle. Contrary to expectation, large flagellar dispersion during tumbling is not correlated with bacterial escape, since both low and high flagellar dispersions result either in escape from ($\theta < 90°$) or stay at ($\theta > 90°$) the surface. To identify mechanisms that facilitate escape from the surface, we again refer to Appendix B and Fig. 11. There, we show that escaping bacteria have more contacts of their flagella with the surface compared to bacteria that stay near the surface. So, these contacts are clearly relevant for bacteria to escape. Video A8 (ESI†) nicely reveals, how the bacterium uses the flagellar contacts to push itself away from the surface. Another effect is more subtle. The *E. coli* bacterium is a hydrodynamic pusher dipole, which is attracted and then aligns parallel to the surface.[17,19] The dispersion of the flagellar bundle during tumbling certainly weakens the pusher dipole and, therefore, the attraction towards the surface but also its reorientation parallel to the surface.[34] If and how this contributes to bacterial escape, we could not resolve within the current study.

5 Discussion and conclusions

In this article, we numerically investigated an *E. coli* bacterium tumbling both in bulk and near a surface. More specifically, we

examined the role of the surface during tumbling by systematically comparing our observations to those in the bulk fluid. We developed a fine-scale model that captures the mechanical properties of *E. coli*, where flagellar flexibility and polymorphism are modeled using an extended version of Kirchhoff's rod theory. The modeled bacterium swims in an MPCD fluid, which reproduces the flow field generated by the bacterium. We simulated a specific setting of an *E. coli* with four flagella symmetrically attached to the rear of the cell body, which allowed us to concentrate on the influence of tumble time, hook stiffness, and a bounding surface on the tumbling behavior.

First, we investigated a long trajectory in the bulk fluid. During tumbling we observe a systematic drop in velocity followed by strong fluctuations. This velocity drop during tumbling is systematically observed in experiments.[14,40,73] However, only ref. 73 reports the observed velocity fluctuations, which they attribute to a motor reversal without a flagellum leaving the bundle. In our case, the fluctuations are caused by the erratic reorientation of the cell body during tumbling. We quantified reorientation after a single tumble event by calculating the distribution of tumble angles and find good agreement with experiments from Berg and Brown (ref. 14) in the case of a fixed tumble duration. Motivated by the experimental observations of ref. 41, we determined the tumble angle distribution for a tumble duration taken from a Gamma distribution. Although the resulting tumble angle distribution does not fully reproduce experimental observations, we found that *E. coli* needs to reversely rotate a flagellum for at least $10\tau_b$ to exhibit any noticeable reorientation. Thus, such tumbling events could be overlooked in an experiment.

Another important feature of *E. coli* is the flagellar hook, whose high flexibility enables the formation of the flagellar bundle. To study the influence of the hook's bending rigidity,[32,33] we investigated bacterial tumbling with an increasingly stiffer hook. For a flexible hook, the bundle can become highly dispersed during tumbling, which is also observed in experiments.[11,41,73] However, increasing its bending rigidity systematically reduces flagellar dispersion, which we quantify by the smallest eigenvalue of the moment of inertia tensor. A stiffer hook hinders the rotation of both the reversely rotating flagellum and the cell body. We observe a more narrow tumble angle distribution with a larger mean tumble angle compared to the reference case. In particular, the reversely rotating flagellum protrudes more clearly from a tighter bundle, which agrees more with the traditional view of a tumble event. In ref. 33 and 45 it is argued that this enhances tumbling. Still, further experimental and theoretical investigations are needed to further elucidate the determining features of tumbling.

When immersed in a fluid bounded by two parallel no-slip walls, we observe significantly smaller tumble angles, as also reported in several experiments.[39–41] A more detailed investigation reveals a tendency for the bacterium to reorient parallel to the wall, while the rate for swimming away from the surface is 53%. The conditions leading to a successful escape are nontrivial. One observation from our simulations is that the

bacterium seems to use direct contact between the flagella and the surface to push itself away from the wall. Furthermore, during tumbling the pusher flow field, which attracts the *E. coli* to the surface, is certainly weakened by the dispersed flagellar bundle. However, we did not find a clear correlation between the bacterial escape and bundle dispersion. Nevertheless, to decide whether hydrodynamic effects play a role for bacterial escape during tumbling, a detailed investigation of the flow field generated by *E. coli* is required, which is beyond what the current study can deliver. We found a predominance of small in-plane reorientations near the surface. This observation could explain the apparent suppression of tumbling as reported in ref. 39, since small in-plane reorientations are harder to detect. Finally, a pronounced in-plane reorientation is correlated with a larger flagellar dispersion.

Our results demonstrate that bacteria move on long trajectories close to a surface despite tumbling. This supports bacterial adhesion and ultimately the formation of biofilms. Thus, external mechanisms need to be explored to prevent bacteria from staying at surfaces. For instance, ref. 75 showed that shear flow can promote bacterial escape from surfaces, suggesting a possible strategy to mitigate surface accumulation. In addition, a recent study investigated the role of undulating surfaces in controlling bacterial trapping and found that bacteria accumulate in sufficiently deep valleys.[76]

Our model does not account for biophysical processes that govern behavioral variability, as detailed in ref. 41. Also, for our systematic study to explore the effect of a surface on tumbling, we modeled the bacterium with four symmetrically attached flagella. However, the number and arrangement of the flagella varies largely. While this has only a minor influence on swimming speed,[48] the influence on tumbling needs further investigation.

In summary, we developed a detailed model of an *E. coli* bacterium tumbling in bulk and near a surface. Our study provides new insights into the role of flagellar dispersion and its influence on the tumble angle distribution. We found good agreement with experimental observations in bulk and suggest that the apparent suppression of tumbling near a surface are due to small in-plane reorientation events that might have been overlooked in experiments. The versatility of our approach opens new avenues for further investigations. For example, the method of MPCD facilitates the implementation of complex environments, such as different flow geometries like Poiseuille flow, curved surfaces, and even model porous systems. Also, the extended Kirchhoff-rod approach can be applied to study other peritrichous bacteria as well as different polymorphic flagellar transformations.

Conflicts of interest

There are no conflicts to declare.

Data availability

The data supporting the findings of this study are available upon request from one of the authors.

Appendices

A Circular swimming of non-tumbling bacteria

We performed simulations of a non-tumbling bacterium swimming near a surface and observed the expected circular trajectory, as demonstrated in Fig. 10. When analyzing the trajectory, we found that the bacterium completed a full circle ($360°$ rotation) in a time of approximately $3700\tau_b$, which corresponds to a rotational rate of about $0.1°/\tau_b$.

B Flagellar collisions with surface

In this section, we quantify the effect of direct flagellar collisions with the surface. In the main text, we highlight their role in the escape process during a tumble event, as illustrated in Video A8 (ESI†). We identify a collision of a flagellar bead with the surface, when the bead approaches the surface with a distance smaller than $\sqrt[6]{2}\sigma$ so that it experiences the repulsive force from the WCA potential, as described in eqn (5). In 300 equally spaced simulation snapshots of a tumble event, which we stored during a simulation run, we identify for each bead i the number of collisions n_i, averaged over all four flagella and all the simulation runs used to determine the tumble angle distribution. Then, we construct the probability distribution $P_i = n_i/300$ giving the probability of flagellar bead i to collide with the wall per recorded snapshot.

We distinguish between cases where the *E. coli* model either escapes from or remains near the surface after a tumble event and show their respective probability distribution $P_E(i)$ and $P_S(i)$ in Fig. 11. Summing over all probabilities $P_{E/S}(i)$, gives the probability per snaphot that flagellar beads collide with the surface. This value is below one but for our purpose only the relative values are relevant. So, we find $\sum_{i=1}^{80} P_E(i) = 0.13$ and $\sum_{i=1}^{80} P_S(i) = 0.09$, which reveals a higher probability when the *E. coli* escapes from the surface compared to bacteria that remain near the surface. In both scenarios, collisions of the flagellar tip with the surface occur most frequently, but for the
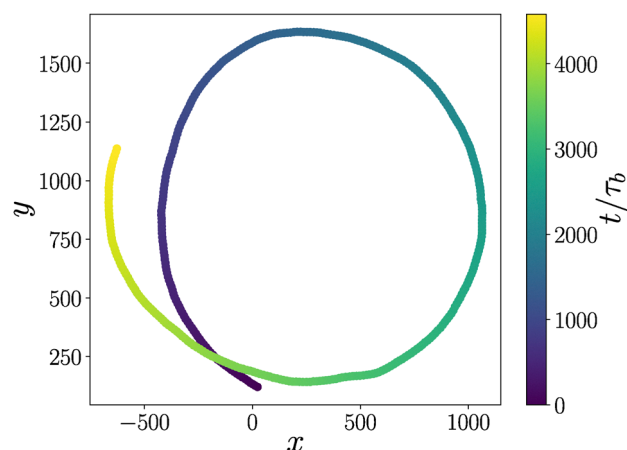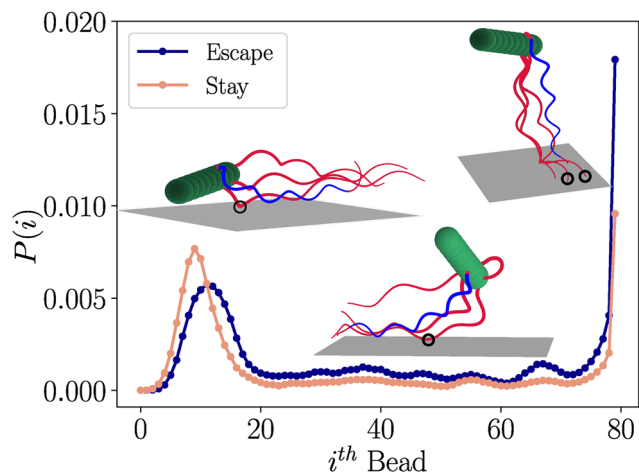

Fig. 10 Circular trajectory of a non-tumbling bacterium. The color encodes time.

Fig. 11 Two probability distributions $P(i)$ showing the likelihood of flagellar bead i to collide with the surface per snapshot during a tumble event. The dark blue curve corresponds to escape events, while the dark salmon curve represents cases where the bacterium remains near the surface. Insets: Three representative snapshots, where the front, middle part, and tip of a flagellum collides with the surface. The collisions are highlighted by black circles.

escaping bacterium the probability is nearly a factor two larger. Collisions of first flagellar beads close to the cell body are systematic in both cases and happen in the early stage of the tumble event. They, may help the bacterium to keep itself away from the surface. Finally, mid-flagellum collisions occur more often when the bacterium escapes from the surface, a feature also observed in Video A8 (ESI†).

Although the mid-flagellum collisions for each bead are more rare, they add up to $\sum_{i=20}^{75} P_{\mathrm{E}}(i) = 0.05$ and $\sum_{i=20}^{75} P_{\mathrm{S}}(i) = 0.02$, which for the escaping bacterium is more than one third of all the collisions. We argue that together with the tip collisions, they play a determining role in the bacterial escape from the surface. As Video A8 (ESI†) demonstrates, the flagella appear to beat against the surface and thereby push the bacterium away from it. This causes a noticeable upward displacement of the bacterium.

Acknowledgements

Notes and references

1 K. M. Ottemann and J. F. Miller, *Mol. Microbiol.*, 1997, **24**, 1109–1117.

2 L. A. Pratt and R. Kolter, *Mol. Microbiol.*, 1998, **30**, 285–293.

3 H. Gest, *Notes Rec. R. Soc. London*, 2004, **58**, 187–201.

4 N. Wadhwa and H. C. Berg, *Nat. Rev. Microbiol.*, 2022, **20**, 161–173.

5 E. Lauga, *Annu. Rev. Fluid Mech.*, 2016, **48**, 105–130.

6 T. Ishikawa, *Annu. Rev. Fluid Mech.*, 2024, **56**, 119–145.

7 D. Bray, *Cell Movements: From Molecules to Motility*, Garland Science, 2nd edn, 2000.

8 P. Watnick and R. Kolter, *J. Bacteriol.*, 2000, **182**, 2675–2679.

9 H. C. Berg and L. Turner, *Biophys. J.*, 1993, **65**, 2201–2216.

10 H. C. Berg, *Annu. Rev. Biochem.*, 2003, **72**, 19–54.

11 L. Turner, W. S. Ryu and H. C. Berg, *J. Bacteriol.*, 2000, **182**, 2793–2801.

12 H. C. Berg, *E. coli in Motion*, 1st edn, 2004.

13 N. C. Darnton, L. Turner, S. Rojevsky and H. C. Berg, *J. Bacteriol.*, 2007, **189**, 1756–1764.

14 H. C. Berg and D. A. Brown, *Nature*, 1972, **239**, 500–504.

15 J. W. Costerton, Z. Lewandowski, D. E. Caldwell, D. R. Korber and H. M. Lappin-Scott, *Annu. Rev. Microbiol.*, 1995, **49**, 711–745.

16 R. Van Houdt and C. W. Michiels, *Res. Microbiol.*, 2005, **156**, 626–633.

17 A. P. Berke, L. Turner, H. C. Berg and E. Lauga, *Phys. Rev. Lett.*, 2008, **101**, 038102.

18 G. Li, J. Bensson, L. Nisimova, D. Munger, P. Mahautmr, J. X. Tang, M. R. Maxey and Y. V. Brun, *Phys. Rev. E: Stat., Nonlinear, Soft Matter Phys.*, 2011, **84**, 041932.

19 K. Drescher, J. Dunkel, L. H. Cisneros, S. Ganguly and R. E. Goldstein, *Proc. Natl. Acad. Sci. U. S. A.*, 2011, **108**, 10940–10945.

20 R. Vogel and H. Stark, *Phys. Rev. Lett.*, 2013, **110**, 158104.

21 T. C. Adhyapak and H. Stark, *Soft Matter*, 2016, **12**, 5621–5629.

22 C. R. Calladine, *Nature*, 1975, **255**, 121–124.

23 T. C. Adhyapak and H. Stark, *Phys. Rev. E: Stat., Nonlinear, Soft Matter Phys.*, 2015, **92**, 052701.

24 W. Lee, Y. Kim, B. E. Griffith and S. Lim, *Phys. Rev. E*, 2018, **98**, 052405.

25 E. E. Riley, D. Das and E. Lauga, *Sci. Rep.*, 2018, **8**, 10728.

26 K. Son, J. S. Guasto and R. Stocker, *Nat. Phys.*, 2013, **9**, 494–498.

27 T. Hirano, S. Yamaguchi, K. Oosawa and S. Aizawa, *J. Bacteriol.*, 1994, **176**, 5439–5449.

28 T. Kato, F. Makino, T. Miyata, P. Horváth and K. Namba, *Nat. Commun.*, 2019, **10**, 5295.

29 M. T. Brown, B. C. Steel, C. Silvestrin, D. A. Wilkinson, N. J. Delalez, C. N. Lumb, B. Obara, J. P. Armitage and R. M. Berry, *J. Bacteriol.*, 2012, **194**, 3495–3501.

30 S. Bianchi, F. Saglimbeni, G. Frangipane, M. C. Cannarsa and R. Di Leonardo, *PRX Life*, 2023, **1**, 013016.

31 I. Spöring, V. A. Martinez, C. Hotz, J. Schwarz-Linek, K. L. Grady, J. M. Nava-Sedeño, T. Vissers, H. M. Singer, M. Rohde, C. Bourquin, H. Hatzikirou, W. C. K. Poon, Y. S. Dufour and M. Erhardt, *PLoS Biol.*, 2018, **16**, 1–19.

32 A. L. Nord, A. Biquet-Bisquert, M. Abkarian, T. Pigaglio, F. Seduk, A. Magalon and F. Pedaci, *Nat. Commun.*, 2022, **13**, 2925.

33 X. Zhang, C. Zhang, R. Zhang and J. Yuan, *Phys. Rev. Lett.*, 2023, **130**, 138401.

34 K. Schaar, A. Zöttl and H. Stark, *Phys. Rev. Lett.*, 2015, **115**, 038101.

35 S. M. Mousavi, G. Gompper and R. G. Winkler, *Soft Matter*, 2020, **16**, 4866–4875.

36 E. Lauga, W. R. DiLuzio, G. M. Whitesides and H. A. Stone, *Biophys. J.*, 2006, **90**, 400–412.

37 E. Perez Ipiña, S. Otte, R. Pontier-Bres, D. Czerucka and F. Peruani, *Nat. Phys.*, 2019, **15**, 610–615.

38 S. Bianchi, F. Saglimbeni and R. Di Leonardo, *Phys. Rev. X*, 2017, **7**, 011010.

39 M. Molaei, M. Barry, R. Stocker and J. Sheng, *Phys. Rev. Lett.*, 2014, **113**, 068103.

40 L. Lemelle, T. Cajgfinger, C. C. Nguyen, A. Dominjon, C. Place, E. Chatre, R. Barbier, J.-F. Palierne and C. Vaillant, *Biophys. J.*, 2020, **118**, 2400–2410.

41 G. Junot, T. Darnige, A. Lindner, V. A. Martinez, J. Arlt, A. Dawson, W. C. K. Poon, H. Auradou and E. Clément, *Phys. Rev. Lett.*, 2022, **128**, 248101.

42 D. Giacché, T. Ishikawa and T. Yamaguchi, *Phys. Rev. E: Stat., Nonlinear, Soft Matter Phys.*, 2010, **82**, 056309.

43 J. Hu, A. Wysocki, R. G. Winkler and G. Gompper, *Sci. Rep.*, 2015, **5**, 9586.

44 M. Kong, Y. Wu, G. Li and R. G. Larson, *Soft Matter*, 2015, **11**, 1572–1581.

45 B. Wu-Zhang, P. Zhang, R. Baillou, A. Lindner, E. Clément, G. Gompper and D. A. Fedosov, *J. R. Soc. Interface*, 2025, **22**, 20250035.

46 M. Dvoriashyna and E. Lauga, *PLoS ONE*, 2021, **16**, 1–26.

47 A. Zöttl and H. Stark, *Eur. Phys. J. E: Soft Matter Biol. Phys.*, 2018, **41**, 61.

48 J. Hu, M. Yang, G. Gompper and R. G. Winkler, *Soft Matter*, 2015, **11**, 7867–7876.

49 S. B. Babu and H. Stark, *New J. Phys.*, 2012, **14**, 085012.

50 A. W. Zantop and H. Stark, *Soft Matter*, 2020, **16**, 6400–6412.

51 T. Eisenstecken, J. Hu and R. G. Winkler, *Soft Matter*, 2016, **12**, 8316–8326.

52 L. D. Landau and E. M. Lifshitz, *Theory of Elasticity*, 3rd edn, 1976.

53 A. E. H. Love, *A treatise on the mathematical theory of elasticity*, Cambridge University Press, 2013.

54 R. Vogel and H. Stark, *Eur. Phys. J. E: Soft Matter Biol. Phys.*, 2010, **33**, 259–271.

55 R. Vogel and H. Stark, *Eur. Phys. J. E: Soft Matter Biol. Phys.*, 2012, **35**, 15.

56 R. E. Goldstein, A. Goriely, G. Huber and C. W. Wolgemuth, *Phys. Rev. Lett.*, 2000, **84**, 1631–1634.

57 P. J. Mears, S. Koirala, C. V. Rao, I. Golding and Y. R. Chemla, *eLife*, 2014, **3**, e01916.

58 K. Namba and F. Vonderviszt, *Q. Rev. Biophys.*, 1997, **30**, 1–65.

59 A. Malevanets and R. Kapral, *J. Chem. Phys.*, 1999, **110**, 8605–8613.

60 A. Malevanets and R. Kapral, *J. Chem. Phys.*, 2000, **112**, 7260–7269.

61 G. Gompper, T. Ihle, D. Kroll and R. Winkler, in *Multi-Particle Collision Dynamics: A Particle-Based Mesoscale Simulation Approach to the Hydrodynamics of Complex Fluids*, ed. C. Holm and K. Kremer, Springer Berlin Heidelberg, Berlin, Heidelberg, 2009, pp. 1–87.

62 H. Noguchi, N. Kikuchi and G. Gompper, *Europhys. Lett.*, 2007, **78**, 10005.

63 I. O. Götze, H. Noguchi and G. Gompper, *Phys. Rev. E: Stat., Nonlinear, Soft Matter Phys.*, 2007, **76**, 046705.

64 T. Ihle and D. M. Kroll, *Phys. Rev. E: Stat., Nonlinear, Soft Matter Phys.*, 2001, **63**, 020201.

65 H. Noguchi and G. Gompper, *Phys. Rev. E: Stat., Nonlinear, Soft Matter Phys.*, 2008, **78**, 016706.

66 M. Ripoll, K. Mussawisade, R. G. Winkler and G. Gompper, *Phys. Rev. E: Stat., Nonlinear, Soft Matter Phys.*, 2005, **72**, 016701.

67 N. C. Darnton and H. C. Berg, *Biophys. J.*, 2007, **92**, 2230–2236.

68 A. Sen, R. K. Nandy and A. N. Ghosh, *J. Electron Microsc.*, 2004, **53**, 305–309.

69 J. K. Dhont, *An Introduction to Dynamics of Colloids*, Elsevier, Amsterdam, 1996, vol. 2.

70 Z. Qu, F. Z. Temel, R. Henderikx and K. S. Breuer, *Proc. Natl. Acad. Sci. U. S. A.*, 2018, **115**, 1707–1712.

71 M. Seyrich, Z. Alirezaeizanjani, C. Beta and H. Stark, *New J. Phys.*, 2018, **20**, 103033.

72 F. Bai, R. W. Branch, D. V. Nicolau, T. Pilizota, B. C. Steel, P. K. Maini and R. M. Berry, *Science*, 2010, **327**, 685–689.

73 L. Turner, L. Ping, M. Neubauer and H. C. Berg, *Biophys. J.*, 2016, **111**, 630–639.

74 J. Saragosti, P. Silberzan and A. Buguin, *PLoS ONE*, 2012, 7, 1–6.

75 M. Molaei and J. Sheng, *Sci. Rep.*, 2016, **6**, 35290.

76 B. Pérez-Estay, M. L. Cordero, N. Sepúlveda and R. Soto, *Phys. Rev. E*, 2024, **109**, 054601.